



Research paper

Synthesis of “sea urchin”-like carbon nanotubes/porous carbon superstructures derived from waste biomass for treatment of various contaminants



Yunjin Yao^{a,b,*}, Chao Lian^a, Guodong Wu^a, Yi Hu^a, Fengyu Wei^a, Maojing Yu^a, Shaobin Wang^{c,**}

^a Anhui Province Key Laboratory of Advanced Catalytic Materials and Reaction Engineering, School of Chemistry and Chemical Engineering, Hefei University of Technology, Tunxi Road 193, Hefei 230009, China

^b School of Chemistry and Material Science, University of Science and Technology of China, Hefei 230026, China

^c Department of Chemical Engineering, Curtin University, G.P.O. Box U1987, Perth, Western Australia 6845, Australia

ARTICLE INFO

Article history:

Received 17 April 2017

Received in revised form 17 June 2017

Accepted 24 July 2017

Available online 25 July 2017

Keywords:

Carbon nanotubes

Biomass

Hexavalent chromium

Organic pollutants

Heterogeneous catalysis

ABSTRACT

Novel “sea urchin”-like Ni nanoparticles embedded in N-doped carbon nanotubes (CNTs) supported on porous carbon (Ni@N-C) 3D materials derived from waste biomass were prepared via pyrolysis and employed as an environmentally friendly, easy available and cost-effective catalyst for removal of toxic pollutants. The characterizations indicated that Ni⁰ catalyzed the growth of intertwined CNTs on carbon layers, affording abundant porous structures and larger specific surface area. With the synergistic effect of embedded Ni⁰ nanoparticles, nitrogen doping, hierarchical micro-mesopores, and interconnected CNTs, Ni@N-C displayed a superior catalytic capability for the oxidation of organic pollutants using peroxymonosulfate as an oxidant, and catalytic reduction of toxic Cr^{VI} to nontoxic Cr^{III} by formic acid as a reducing agent. It was found that pyrolysis temperatures affected the compositions, morphologies, and catalytic properties of Ni@N-C. Inactive oxidized N species have transformed to the highly active graphitic N, pyridinic-N, and Ni-O-N clusters, thereby improving the catalytic activity. Moreover, Ni@N-C maintained good physicochemical structure and stable activity even after several cycles of reactions. The simple synthetic strategies, 3D structure, and remarkable performance of Ni@N-C composites make them serve as alternative environmentally friendly catalysts for removal of pollutants.

© 2017 Elsevier B.V. All rights reserved.

1. Introduction

Toxic pollutants like reactive dyes and hexavalent chromium (Cr^{VI}) presented in water streams have attracted significant research attention because of their toxicity, slow self-degradation in nature, and huge volume of production from various industries [1–5]. Unfortunately, conventional technologies such as filtration, liquid extraction, biological treatment, chemical oxidation, and membrane process have some disadvantages including insufficient capacities, slow reaction rates, and low selectivity [1,6]. Thus, it has become a challenge in the development of effective materi-

als and/or methods with an excellent performance to capture and remove these toxic species from waters [7–10].

Recently, much research has focused on carbon-based catalysis, an effective and ideal technique, to eliminate the aqueous contaminants. Carbon materials including metal carbides (such as Ni_xC, Fe_xC, Co_xC etc.) and heteroatom (such as nitrogen, phosphorus, sulfur, and boron, etc.) -doped porous carbons are ubiquitous in environment-related applications because of their superior properties and wide availability [11,12]. Although metal carbides are abundant and nonprecious, it is highly challenging to solve the problems of sintering or leaching of metals, which causes irreversible deactivation of the catalysts [13]. Metal nanoparticles (NPs) embedded in carbon shells are highly promising and active materials with high stability, because the carbon shells protect the metal NPs. In our previous studies, Fe embedded in N-doped carbon nanotubes (CNTs) has been demonstrated as the heterogeneous catalyst to generate radicals from peroxymonosulfate (PMS, HSO₅[−]) for the oxidative degradation of organic wastes [14,15]. Bhowmik

* Corresponding author at: School of Chemistry and Chemical Engineering, Hefei University of Technology, Tunxi Road 193, Hefei, 230009, China.

** Corresponding author.

E-mail addresses: yaoyunjin@gmail.com (Y. Yao), shaobin.wang@curtin.edu.au (S. Wang).

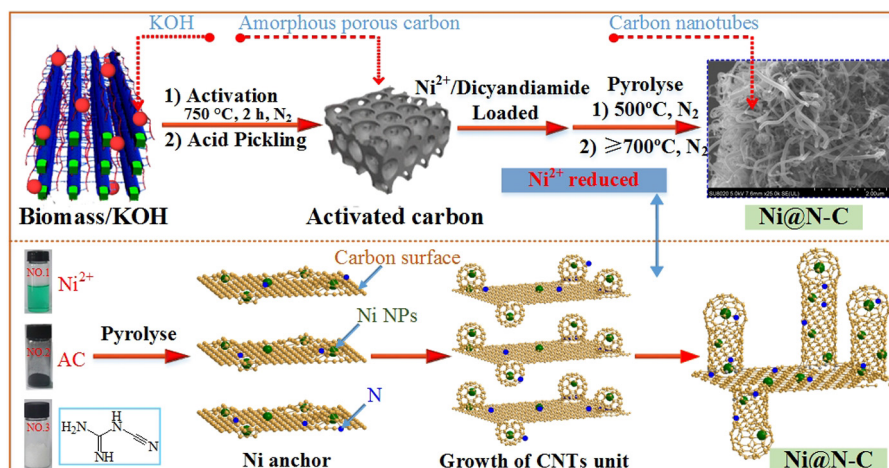


Fig. 1. Schematic illustration for the synthesis of Ni@N-C catalysts.

et al. [16] reported Ni NPs stabilized by reduced graphene oxide as heterogeneous catalysts to reduce toxic Cr^{VI} compounds to non-toxic Cr^{III} by formic acid as a reducing agent. It was supposed to possess the features of fast mass transport channels and abundant active sites [17]. Unfortunately, most reported materials have a low activity or stability. Hence, there is still a need to explore rationally designed architectures as the heterogeneous catalysts in water treatment.

Three-dimensional (3D) carbon-based structures have recently attracted enormous interest, due to their unique properties including high porosity, electrical conductivity, and specific surface area, which are beneficial to efficient diffusion/mass transfer of liquid/solid phase [18,19]. They are also more easily separated because of their larger size and weaker Brownian motion [20]. Numerous techniques have been developed to prepare porous 3D carbon materials, including templating, combustion, cathodic corrosion, and aerogel formation [21]. For example, Wan et al. [22] synthesized superparamagnetic $\gamma\text{-Fe}_2\text{O}_3$ NPs encapsulated in 3D cellulose aerogels for Cr^{VI} removal. However, the harmful and expensive precursors (graphene or CNTs) or complex equipment involved in these syntheses have impeded their commercialization. The development of more efficient and stable catalysts using renewable precursors in a cost-effective manner is highly desirable for a successful large-scale application.

Nowadays, there is a trend to produce carbon-based materials derived from biomass, as they are very cheap, extensively available, accessible, and recyclable, etc. Many efforts have been made to increase the catalytic performance of biomass-derived carbons. Transition metals (Fe, Co, Ni, etc.) coordinated with nitrogen doping in CNTs from biomass have been extensively studied because of their low cost, long durability and superior catalytic activity. For example, N-doped graphene encapsulating Fe_3C was synthesized by Shi et al. [23] via calcination of biomass/melamine/ FeCl_3 in N_2 atmosphere. Intrinsic properties and unique structure, such as high chemical stability, surface area, and electrical conductivity, make them extremely attractive as catalytic materials. The incorporation of embedded metal NPs and nitrogen doping in CNTs is an interesting approach to synergistically improve active sites [21]. Thus, developing Ni embedded N-doped CNTs with an excellent activity from waste biomass has motivated our curiosity. In addition, recycling of waste biomass provides extra values for contaminant treatment.

Herein, we demonstrated a scalable strategy for the controlled synthesis of “sea urchin”-like nickel embedded in N-doped CNTs-supported on porous carbon (Ni@N-C) as a 3D catalyst through pyrolysis treatment of a waste carbon precursor, dicyandiamide

and $\text{NiCl}_2 \cdot 6\text{H}_2\text{O}$. The catalytic performances of Ni@N-C composites were evaluated by the oxidation of Orange II using PMS as an oxidant, and the catalytic reduction of Cr^{VI} to Cr^{III} by formic acid as the reducing agent. As expected, Ni@N-C exhibited catalytic activity and long-term stability under acidic conditions. The prominent catalytic performance and low production cost render Ni@N-C as a promising candidate in green catalysis.

2. Materials and Methods

2.1. Synthesis of Ni@N-C catalysts

A biomass (stillage residue, a waste from the liquor industry) was obtained from Anhui Yingjia Gongjiu Corp, China. Before use, the biomass was washed, dried, crushed, and sieved to 0.15–0.30 mm. The biomass powder was activated with a KOH activation process as reported in our previous study [24]. Typically, the raw biomass was mixed with KOH (biomass/KOH mass ratio as 1/1) and then annealed in high purity N_2 atmosphere at 750°C for 2 h. The resulted samples were washed with HCl solution and distilled water until neutral filtrate, and then dried at 70°C for 24 h. The obtained porous activated carbon was denoted as AC.

The process used to prepare Ni@N-C catalysts is shown in Fig. 1. Typically, 0.2 g AC and 0.0476 mol dicyandiamide were then immersed into 200 mL aqueous solution of $\text{NiCl}_2 \cdot 6\text{H}_2\text{O}$ (5.0 mM) with stirring for 12 h. Then, the solvent solution was slowly evaporated. Subsequently, the obtained powders were annealed in N_2 atmosphere at 500°C for 2 h to obtain reduced Ni catalysts and then further annealed at the setting temperatures (700°C , 800°C , and 900°C) for another 2 h to obtain Ni@N-C composites. The powder collected was filtered, washed, and dried to get the catalyst materials. The obtained products were denoted as Ni@N-C-T, where T represents the pyrolysis temperatures ($T = 700^\circ\text{C}$, 800°C , or 900°C).

2.2. Characterizations

The phase structures of the Ni@N-C catalysts were analyzed by an X'Pert PRO Multi-purpose XRD System using $\text{Cu K}\alpha$ radiation. Raman spectra were recorded at ambient temperature on a confocal Raman microscope (Horiba Jobin Yvon LabRAM Aramis) with 532 nm wavelength laser. Fourier transform infrared (FT-IR) spectra were obtained on a Perkin-Elmer Spectrum 100 spectrometer in the range of $400\text{--}4000\text{ cm}^{-1}$, and X-ray photoelectron spectroscopic (XPS) measurements were performed using an ESCALAB250 instrument. The morphology and elemental composition of the Ni@N-C catalysts were obtained by field

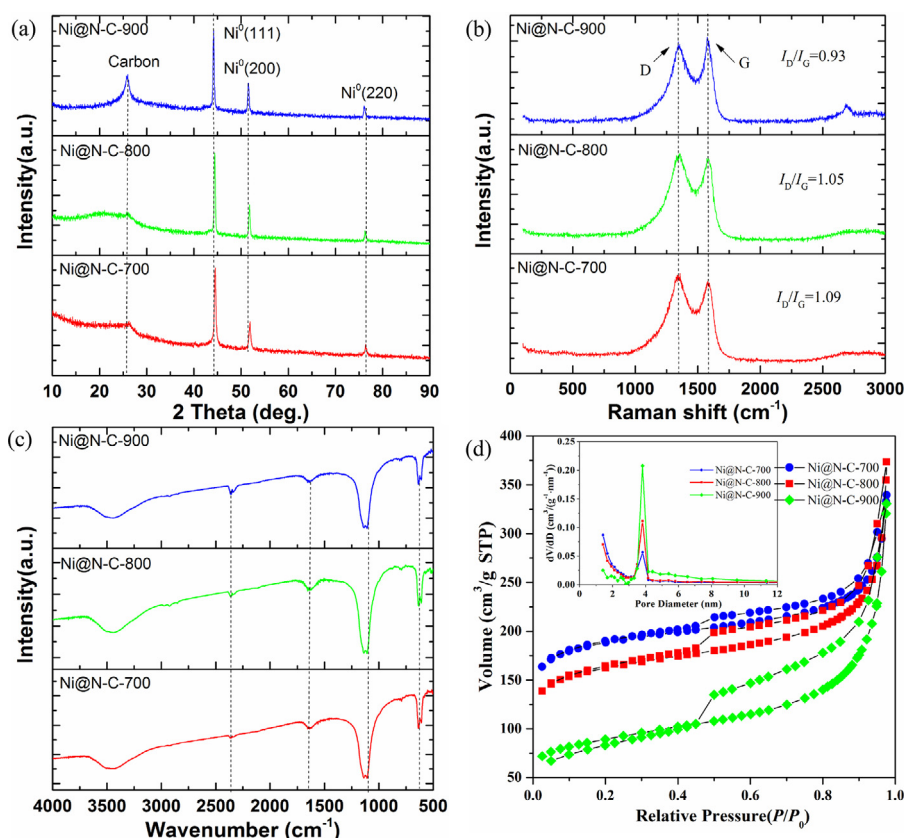


Fig. 2. (a) XRD patterns, (b) Raman and (c) FT-IR spectra, (d) Nitrogen sorption isotherms of different Ni@N-C composites with different pyrolysis temperatures. Inset: Pore size distribution.

emission scanning electron microscopy (FESEM; Hitachi SU8020), field-emission transmission electron microscopy (FETEM, Jeol JEM 2100F), and high resolution TEM (HRTEM) with elemental mapping analysis and energy-dispersive X-ray spectroscopy (EDS). The Brunauer-Emmett-Teller (BET) surface area and pore structure of samples were obtained from N₂ adsorption/desorption isotherms at −196 °C using a Builder 4200 instrument (Tristar II 3020 M, Micromeritics Instrument Corp., USA).

2.3. Catalytic evaluation

The catalytic activity for organic degradation was tested in a 250 mL beaker. The catalysts (10 mg) were dispersed into organic dye solutions (200 mL) with the desired initial concentrations. The well-mixed solution was stirred in dark for 120 min to attain adsorption equilibrium, followed by addition of the oxidant (PMS, 0.05–0.25 g/L) for reaction. Later, 2.0 mL of solution samples were taken out at given time intervals, separated with a magnet for analysis. The catalyst stability was checked by recovering the solid through filtration, washing, drying at 80 °C, and retested in the following cycle. In some experiments, the scavenger chemicals were also used specifically to verify the radical species.

The organic concentrations were obtained by a UV–vis spectrophotometer. Chemical oxygen demand (COD) was measured with an analyzer (DR1010, Hach Co., Loveland, CO). The metal ion leaching was carried out using atomic absorption spectroscopy (AAS, AA800, Perkin-Elmer). The reactive radicals were trapped with 5,5-dimethyl-1-pyrroline N-oxide (DMPO, >99 wt%) and measured using electron spin resonance (ESR, JES-FA200, Japan). Samples were collected from the Orange II degradation system in the presence of PMS and Ni@N-C catalyst within different contact time.

For the catalytic reduction of Cr^{VI}, potassium dichromate (K₂Cr₂O₇) was the source of Cr^{VI} and HCOOH was the electron donor under an acidic solution. The batch experiments were carried out in a stirred batch-fed beaker at room temperature. Typically, a 200 mL aqueous reaction mixture was prepared by mixing K₂Cr₂O₇ and deionized water to make a solution at a desired concentration. Subsequently, the Cr^{VI} reduction was initiated by the sequential addition of Ni@N-C catalyst and HCOOH. Then, a certain volume of the solution was sampled at given time intervals, and then filtered (0.22 μm, PTFE) to remove the catalyst solids. The Cr^{VI} content in the reaction solution was monitored by measuring UV–vis absorbance of K₂Cr₂O₇ at 350 nm. After each experiment, the Ni@N-C composite was magnetically captured on the bottom of flasks, washed with water, and dried before the next catalytic cycle.

3. Results and discussion

3.1. Catalyst characterizations

XRD spectra of Ni@N-C composites (Fig. 2a) show the diffraction peaks at $2\theta \approx 26.2^\circ$, attributing to the (002) reflection of graphitic carbon. In addition, the intensity of this reflection increases with pyrolysis temperatures, which may be due to the fact that Ni@N-C loses some functional groups at a high temperature [23]. In addition to the characteristic peaks from carbon, the diffraction peaks at around 44.2° , 51.7° and 76.2° can be indexed to the (111), (200) and (220) crystalline planes of Ni⁰ (PDF no. 65-0380), respectively, suggesting the successful reduction of nickel ions to a metallic state during the pyrolysis process [25,26]. The Raman spectra contain characteristic wide D and G bands at approximate 1343 and 1577 cm^{−1}, respectively (Fig. 2b). The intensity ratio of the D and G bands (I_D/I_G) is used to estimate the degree of graphitization.

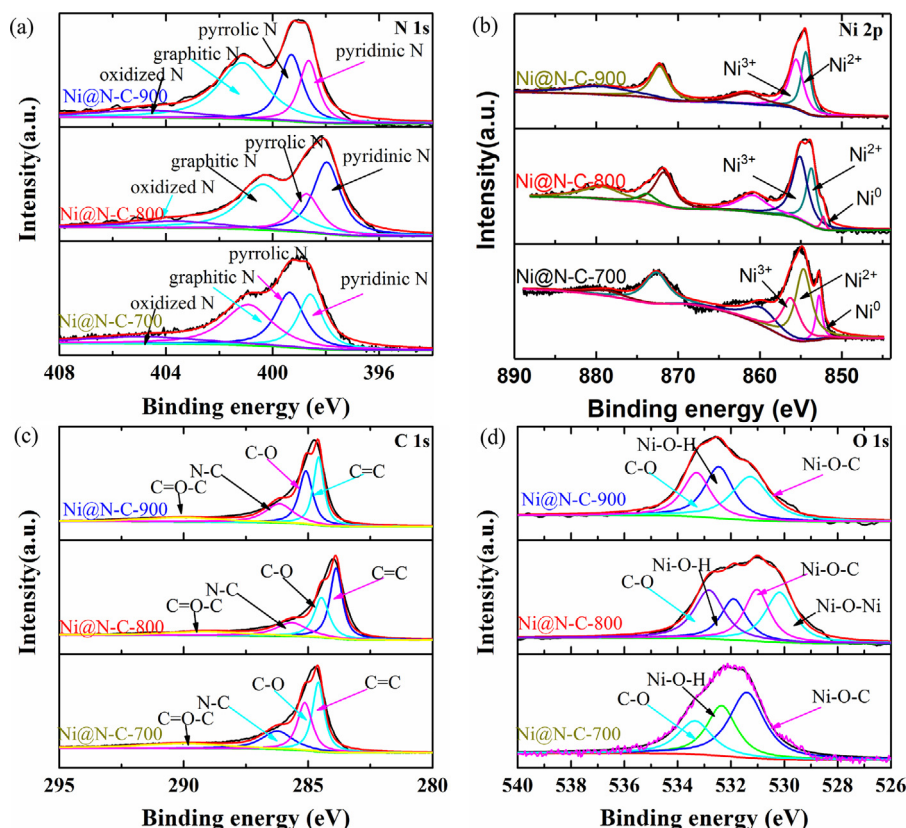


Fig. 3. (a) N 1s, (b) Ni 2p, (c) C 1s, (d) O 1s XPS of different Ni@N-C composites.

The ratio values of Ni@N-C-700, Ni@N-C-800, and Ni@N-C-900 are 1.09, 1.05, and 0.93, respectively. This reveals that the degree of crystallinity of Ni@N-Cs increases with increasing temperatures [27].

FT-IR spectroscopy (Fig. 2c) indicates the broad peaks centered at 2924 and 3440 cm^{-1} , which are attributed to $-\text{CH}$ and $-\text{OH}$ stretching vibrations, respectively, while the peaks at 1108 and 1139 cm^{-1} are attributed to $\text{C}-\text{OH}$ and $\text{C}-\text{N}$ stretching vibrations, respectively [28,29]. The peak locating at 1636 cm^{-1} is attributed to $\text{N}-\text{H}$ vibration coupled with $\text{C}-\text{N}$ stretching mode [30]. Furthermore, the peak at 636 cm^{-1} typically fits in $\text{Ni}-\text{O}$ bond vibration. The N_2 adsorption/desorption isotherms are shown in Fig. 2d. The shape of the physisorption isotherm is in accordance with type IV hysteresis loop in a P/P_0 range of 0.45–0.98, the typical characteristics of mesoporous structure according to the IUPAC classification [31]. The pore size distribution was analyzed, revealing the mesopores and abundant micropores (Table S1). The surface areas are 558 $\text{m}^2 \text{g}^{-1}$ for Ni@N-C-700, 487 $\text{m}^2 \text{g}^{-1}$ for Ni@N-C-800, and 283 $\text{m}^2 \text{g}^{-1}$ for Ni@N-C-900, respectively, decreasing with the increase of the pyrolysis temperatures.

The effect of calcination temperatures on the chemical composition and element bonding configurations of the synthesized materials was also revealed by XPS analysis. The high-resolution N 1s XPS spectra (Fig. 3a) can be deconvoluted into four different peaks at ~ 398.6 , ~ 399.4 , ~ 400.9 , and ~ 404.8 eV, attributing to pyridinic N (or $\text{Ni}-\text{N}$ bonding), pyrrolic N, graphitic N (or quaternary N), and oxidized N, respectively [32,33]. Upon annealing at high temperatures, the amount of graphitic N increased whereas the content of pyridinic N initially increased and then decreased, resulting in the fractions of each N-configuration changing accordingly. As reported in previous literatures [23], pyridinic N and graphitic N were conducive for enhanced catalytic performance in oxygen reduction reaction because they could reduce the energy

barrier and accelerate the electron transfer. The XPS spectra of Ni 2p (Fig. 3b) clearly demonstrate metallic Ni at ~ 852.8 eV, along with NiO (~ 854.7 eV) and $\text{Ni}-\text{O}-\text{N}$ (~ 856.3 eV) [34–36]. In comparison, no obvious XPS signal of Ni^0 at 852.8 eV is observed for Ni@N-C-900, implying that Ni^0 NPs are encapsulated by the carbon layers. The peaks in C 1s spectrum deconvoluted (Fig. 3c) at ~ 284.6 , ~ 285.1 , ~ 286.3 , and ~ 289.9 eV are referred to carbon ring $\text{C}=\text{C}$, $\text{C}-\text{O}$, NC , and $\text{C}=\text{O}-\text{C}$ bonds, respectively [18,36]. Similarly, the species in O 1s spectrum of samples (Fig. 3d) are ascribed to $\text{Ni}-\text{O}-\text{C}$ (~ 531.5 eV), $\text{Ni}-\text{O}-\text{H}$ (~ 532.3 eV) and $\text{C}-\text{O}$ (~ 533.4 eV), while a new peak at ~ 530.2 eV in Ni@N-C-800 suggests a possible $\text{Ni}-\text{O}-\text{Ni}$ bond on the Ni@N-C-800 interface [36,37]. The results indicate that pyrolysis temperature is a primary factor influencing the microstructure of Ni@N-C.

FESEM images of Ni@N-C composites are presented in Fig. 4a–c. It is seen that a large number of intertwined CNTs anchored on the rough surface of irregular shaped carbon support to produce sea-urchin-like 3D structures. The proportion and diameter of CNTs increased dramatically with increasing calcination temperatures, due to the decomposition of dicyandiamide. Therefore, it is reasonable to speculate that high pyrolysis temperature is more favorable for accelerating the growth of CNTs. FETEM images (Fig. 4d) of Ni@N-C-700 confirm that plenty of CNTs as bamboo-like structures with the length of 100–300 nm and diameter of around 10–15 nm are grown on the outboard of carbon. More importantly, the HRTEM image (Fig. 4e) confirms that Ni NPs with the diameter between 8 and 26 nm are embedded in the carbon layers, which can be ascribed to the catalytic effect of the Ni nano-catalyst during the carbonization process [25]. Metallic NPs are crystalline, and the lattice spacings of ~ 2.05 and 1.77 Å correspond to those of the (111) and (200) planes of Ni^0 , respectively. The graphitic layers of CNTs grown on the surface of Ni@N-C-700 are not parallel, indicating the existence of abundant defect sites [38]. Moreover, EDS and elemen-

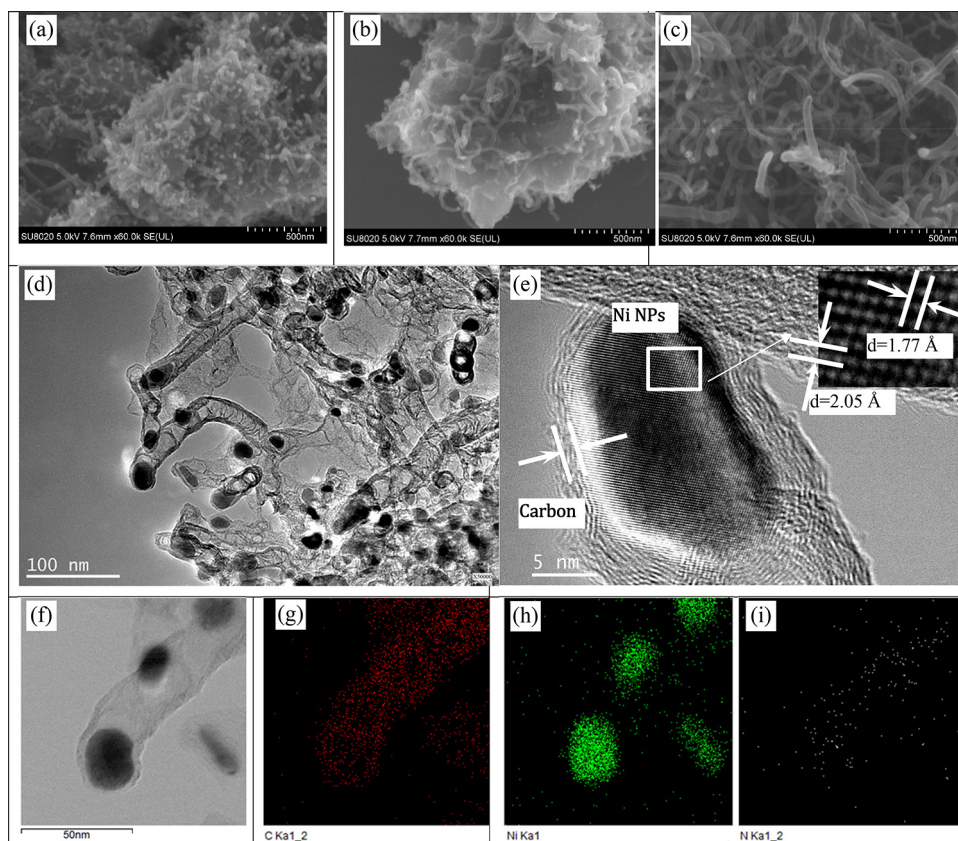


Fig. 4. FESEM images of various Ni@N-Cs: (a) Ni@N-C-700, (b) Ni@N-C-800, and (c) Ni@N-C-900. (d) FETEM image, (e) HRTEM image, and (f–i) EDS mapping of Ni@N-C-700.

tal mapping confirm that Ni@N-C-700 is composed of C, N, Ni, and O elements (Fig. 4f–i and S1). Taken together, these results indicate the formation of Ni@N-C 3D structures with Ni, N codoped CNTs grown on AC sheets.

3.2. Catalytic activity for organics removal

The catalytic performance of Ni@N-C was investigated in catalytic activation of PMS for removal of Orange II. For comparison, CNTs, graphene oxide, Ni^{2+} , Ni^0 and NiO were also tested. Fig. 5a shows that almost no Orange II was removed by PMS alone, meaning PMS itself could hardly oxidize Orange II [39]. As for Ni@N-C performance without the presence of PMS, less than 40% Orange II was removed attributing to adsorption of Orange II onto the Ni@N-C. Once the PMS was added, a sharp drop of Orange II concentration occurred over all the Ni@N-C catalysts, suggesting the PMS was activated. Ni@N-C-700 performed the best activity with almost complete removal (98.2%) of Orange II within 90 min, followed by Ni@N-C-800 and Ni@N-C-900, which removed 96.9% and 68.5% Orange II within 120 min, respectively. These observations suggest that Ni@N-C prepared at lower annealing temperature exhibited greater Orange II removal [40]. Ni@N-C-700 had a larger BET surface area compared to Ni@N-C-800 and Ni@N-C-900 (Table S1). However, as seen in Fig. 5a, the adsorption capacity of Ni@N-C-800 for Orange II was slightly better than Ni@N-C-700. Thus, it is suggested that the adsorption on the as-prepared samples depends not only on the surface area but also on other physicochemical interactions between pollutants and adsorbents. CNTs, graphene oxide, Ni^{2+} , Ni^0 and NiO showed poor performances in PMS activation. Almost no decoloration took place with CNTs, which was significantly different from the previous literature [41,42]. This phenomenon may be explained by the reason that CNTs were commercial samples, which were not pretreated and the surface oxygen species were

high and thus were not quite active. The PMS activation and Orange II degradation involve electron transfer from Orange II (an electron donor) to PMS (an electron acceptor), in which Ni@N-C's engagement as a facile electron transfer mediator is essential [40]. Ni and N atoms can present electrons for a transfer to CNTs surface for reaction, which may be responsible for an improved catalytic activity. Such an electron transfer would be facilitated as Ni@N-C surface serves to bring together electron donor and acceptor pairs to a close proximity. For Ni^0 NPs, there was no electron-transfer mediator to promote the electron transfer, which might explain that pure Ni^0 has not been in a catalytic level compared to that of Ni@N-C. Based on above-mentioned analysis, Ni@N-C exhibits superior chemical activities toward Orange II degradation, attributing to the abundant active sites and effective electron transfer ability.

On the contrary, Ni@N-C could not effectively activate H_2O_2 and peroxydisulfate (PDS), as PMS has a higher oxidizing capability than PDS and H_2O_2 (Fig. 5b). The degradation efficiency of Orange II increased with increasing PMS doses (Fig. 5b) and reaction temperatures in the Ni@N-C/PMS system (Fig. S2). Specially, the intensity of Orange II absorption peak (484 nm) decreased by reflecting in a color change of the solutions (Fig. S3). COD analysis showed that the preadsorption induced 39.2% of COD removal, and the combination of the preadsorption (120 min) and the degradation (120 min) achieved more than 47.8% of COD removal. Apart from Orange II, the degradation of various other pollutants including 4-chlorophenol, rhodamine B, methyl orange, methylene blue, phenol, bisphenol A and methyl violet is shown in Fig. 5c. The degradation of dye-based chemicals such as Orange II, rhodamine B, methylene blue, and methyl orange occurred rapidly; nearly 100% degradation of these pollutants was realized within 120 min. However, under the identical conditions, 4-chlorophenol, phenol, bisphenol A and methyl violet showed a low degradation efficiency, because of the strong

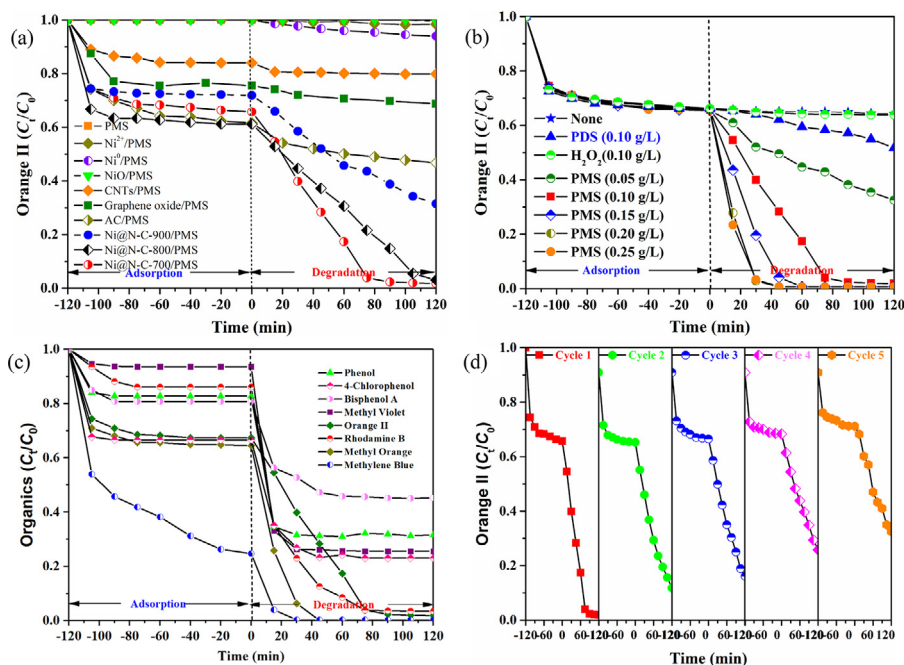


Fig. 5. (a) Catalytic performance of various catalysts mediated by PMS. (b) Orange II degradation mediated by different oxidants. (c) Removal of various organic compounds by the Ni@N-C-700/PMS system. (d) Repeated oxidation of Orange II by the Ni@N-C-700/PMS system. Reaction conditions: [dye] = 20 mg/L, [catalyst] = 50 mg/L, [PMS] = 0.10 g/L, $T = 25^\circ\text{C}$.

persistence of the chemicals. Thus, for those chemicals, it may need more loading of oxidant to achieve high efficiency.

The stability of Ni@N-C catalyst was examined by collecting and reusing in five cycles. As shown in Fig. 5d, after five cycles, 64.2% of its initial activity was still remained. The loss of Ni from the composite was measured by AAS. After each recycle usage, the concentrations of Ni ion in the reaction medium were 0.393, 0.353, 0.277, 0.136, and 0.109 mg/L, respectively. Therefore, it was speculated that the Ni NPs were well protected by the carbon cage. With the increase of the residence time, the adsorption of Orange II on the catalyst surface could decrease accessibility of the active sites and passivate the Ni@N-C surface, resulting in activity deterioration.

To verify the existence of radicals for reactions, we carried out additional experiments using different scavengers, i.e. *tert*-butyl alcohol (*t*-BuOH), 1,4-benzoquinone (BQ), methanol, and dimethyl sulfoxide (DMSO). Methanol has a similar reactivity toward both HO^\bullet and $\text{SO}_4^{\bullet-}$ radicals, with reaction rate constants of $9.7 \times 10^8 \text{ M}^{-1} \text{ s}^{-1}$ and $1.0 \times 10^7 \text{ M}^{-1} \text{ s}^{-1}$, respectively [43]. The alcohol lacking α -hydrogen, e.g. *t*-BuOH, is more selective targeting HO^\bullet radicals, as the rate constant for HO^\bullet radicals ($3.8\text{--}7.6 \times 10^8 \text{ M}^{-1} \text{ s}^{-1}$) is 3 orders of magnitude greater than that for $\text{SO}_4^{\bullet-}$ radicals ($4\text{--}9.1 \times 10^5 \text{ M}^{-1} \text{ s}^{-1}$). As illustrated in Fig. S4a, the addition of *t*-BuOH only partially inhibited Orange II removal. In addition, there was no influence in the presence of methanol compared to the control condition, suggesting that methanol cannot react with surface-adsorbed radicals, because the hydrophilic methanol could not be adsorbed on the Ni@N-C surface (Fig. S4 b) [14,15,24]. Therefore, DMSO was used instead of methanol, which could react with surface-bound HO^\bullet and $\text{SO}_4^{\bullet-}$. Indeed, the degradation of Orange II would be greatly inhibited in the presence of DMSO scavenger (Fig. S4c). However, more increase in the concentration of DMSO scavenger did not show further significant inhibition effects. The possible involvement of other radicals in the oxidation process cannot be ruled out. It was reported previously that $\text{O}_2^{\bullet-}$ has been found to be generated during PMS activation [44]. Therefore, BQ was used as the probing compound of $\text{O}_2^{\bullet-}$ as BQ is more sensitive to $\text{O}_2^{\bullet-}$ than sulfate and hydroxyl radicals [44,45]. In the presence of

BQ, Orange II oxidation was suppressed greatly and high concentrations of the agent resulted in lower degradation, revealing that $\text{O}_2^{\bullet-}$ was also responsible for Orange II decomposition (Fig. S4d). Similar observations were obtained by Cheng et al. [44], which testified the $\text{O}_2^{\bullet-}$ generation via activation of persulfate by CNTs. Therefore, it is deduced that HO^\bullet radicals are more responsible for the degradation with the involvement of sulfate and superoxide radicals.

ESR measurements were performed using DMPO as a trapping agent. As shown in Fig. 6a, the quartet lines with peak strength of 1:2:2:1 and hyperfine coupling constant of $\alpha_N = 1.49 \text{ mT}$ and $\alpha_H = 1.49 \text{ mT}$ could be detected, which accounted for the typical signals of DMPO-HO^\bullet adduct [43]. Moreover, the intensity decreased with increasing reaction time. The hyperfine splitting ($a_N = 0.74 \text{ mT}$ and $a_H = 0.39 \text{ mT}$) was ascribed to 5,5-dimethyl-1-pyrrolidone-2-oxyl or 5,5-dimethylpyrrolidone-2-(oxy)-(1) (DMPO-X) produced via the oxidation of DMPO [46]. A sextet signal with hyperfine coupling parameters ($a_H = 2.28 \text{ mT}$, $a_N = 1.58 \text{ mT}$) was assigned to the DMPO adducts of carbon-based radicals (R^\bullet), which might be responsible for the organic decomposition [47,48]. It is also noted that the signals of $\text{DMPO-SO}_4^{\bullet-}$ and $\text{DMPO-O}_2^{\bullet-}$ were barely detected. This could be explained that $\text{SO}_4^{\bullet-}$ and $\text{O}_2^{\bullet-}$ radicals may quickly transfer to HO^\bullet radical, and thus ESR only detected strong signals of HO^\bullet radical. ESR spectroscopy and sacrificial-reagent incorporated catalysis indicated that HO^\bullet radical was mainly responsible for this persulfate-driven oxidation process.

Thus, from the above results, such a good activity of the prepared Ni@N-C can be attributed to the following factors. Firstly, large amounts of CNTs grown on the carbon surface with a unique 3D structure not only provide highly active sites but also facilitate electron transport along the basal surfaces of the carbon layer. The anchored configuration of Ni@N-C changes the local work function of the AC sheets, making the surface of the carbon layer more active. Secondly, the N-doped carbon layers protect Ni^0 NPs from aggregation and leaching, making them of high stability and activity in the acid condition. This close interconnection between Ni and carbon species hampers the aggregation of Ni NPs and provides a less path suitable for fast electron transfer. Thirdly, the dicynandi-

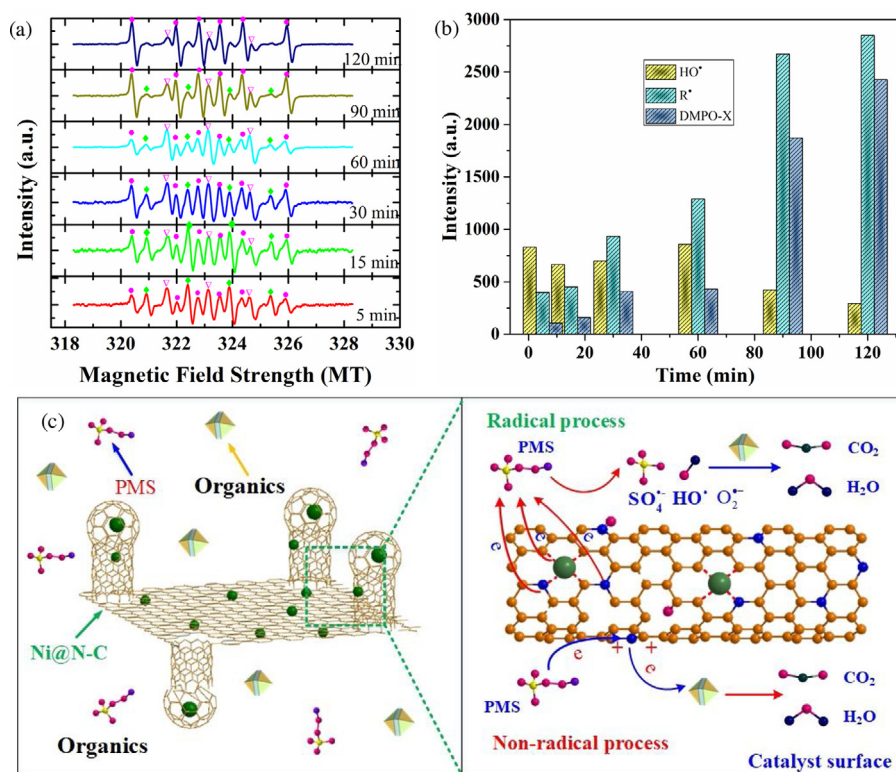


Fig. 6. (a) ESR spectra of PMS activation with DMPO as the trapping agent at different reaction time. (b) Comparison of ESR signal intensity. ▽ represents OH• adduct and • represents carbon-centered adduct. represents DMPO-X. (c) Reaction mechanism for organics removal by the Ni@N-C/PMS system. Reaction conditions: [Orange II] = 20 mg/L, [catalyst] = 50 mg/L, T = 25 °C, [PMS] = 0.10 g/L.

amide and $\text{NiCl}_2 \cdot 6\text{H}_2\text{O}$ doped into the AC precursor indeed enhance the versatile nitrogen of 3D structures. Pyridinic-N, graphitic N, Ni–N clusters, and N dispersed on the Ni@N-C may be responsible for the higher catalytic activity. Furthermore, the high content of micropores and mesopores from biomass-derived porous carbon precursor provides more active sites. Consequently, with the synergistic effect of embedded Ni⁰ NPs, nitrogen doping, hierarchical micro-mesopores, and interconnected CNTs, Ni@N-C exhibits superior heterogeneous catalytic performance.

3.3. Catalytic activity for Cr^{VI} reduction

The catalytic performance of Ni@N-C composites for the transformation of toxic Cr^{VI} to Cr^{III} has been investigated. It was observed that Cr^{VI} reduction did not occur in the presence of only formic acid without a catalyst, which ruled out the possibility of the Cr^{VI} reduction by formic acid solely. When Ni@N-C-800 catalyst was introduced, the absorption peak of Cr^{VI} at 350 nm gradually decreases and finally disappears within 160 min, accompanied with a change in the color from yellow to colorless, indicating the successful reduction of Cr^{VI} to Cr^{III} (Fig. 7a). The Cr^{III} formation was verified by adding excess sodium hydroxide to the solution, resulting in a color change from colorless to green due to the formation of hexahydroxochromate (III) [16,49]. After Cr^{VI} reduction reaction, typical Cr XPS peaks were clearly found on the spent Ni@N-C-800 catalyst (Fig. 7b). The high-resolution XPS spectra of the Cr 2p region show that Cr 2p_{1/2} and Cr 2p_{3/2} peaks are located at ~587.2 and ~577.4 eV, respectively. Each of them could be fitted with two strong peaks, the ones at ~588.1 and ~578.5 eV were assigned to Cr^{VI}, while those at ~586.9 and ~577.2 eV to Cr^{III}, suggesting that Cr^{VI} and Cr^{III} coexisted on the carbon surface. The percentages of Cr^{VI} and Cr^{III} to total Cr species were calculated at 41.2% and 58.8%, respectively.

We further compared the Cr^{VI} reduction performance of different materials, Ni⁰, CNTs, graphene oxide, AC, and Ni@N-C at the different annealing temperatures (Fig. 7c). The Cr^{VI} reduction rates are found to be in an order of CNTs < graphene oxide < Ni⁰ < AC < Ni@N-C-700 < Ni@N-C-900 < Ni@N-C-800. The results clearly show that Ni@N-C-800 is the most active catalyst under our experimental conditions. The change of the annealing temperatures remarkably influenced the activity, attributing to the different material structures (such as, metal content, nitrogen content, nitrogen type, and CNT structure). No noticeable adsorption of Cr^{VI} on Ni@N-C was observed (Fig. S5), indicating that Cr^{VI} was decreased in Ni@N-C/HCOOH, but not adsorbed on the catalyst particles. To confirm the role of HCOOH, the reduction of Cr^{VI} was also studied using formaldehyde, acetic acid, H₂SO₄, citric acid and HCl as reducing agents (Fig. 7d). The Cr^{VI} reduction rates for different reducing agents follow an order of formaldehyde < acetic acid < H₂SO₄ < HCl < citric acid < HCOOH, which means that HCOOH can be a potential reducing agent for Cr^{VI} reduction.

To check the process viability of Ni@N-C/HCOOH catalytic system, reduction of Cr^{VI} was repeated up to four cycles (Fig. 8a). The removal efficiency of Cr^{VI} gradually decreases with increasing cycles because the surface of Ni@N-C is preadsorbed with in situ generated Cr^{III}. These results once again prove that Ni@N-C/HCOOH system is a practical method for Cr^{VI} removal. The stability of the Ni@N-C catalysts was also examined by XRD and XPS measurements. The XRD patterns and XPS spectra of the recovered spent catalysts shown in Fig. S6 and S7 are identical to the fresh catalyst, which indicates that the structure of the catalyst remained stable even after repeated experimental runs, clearly demonstrating the high stability of Ni@N-C catalysts. The introduction of a trace amount of ascorbic acid (0.568 mM), known as a better electron donor, could enhance reductive conversion of Cr^{VI} (Fig. S8). This

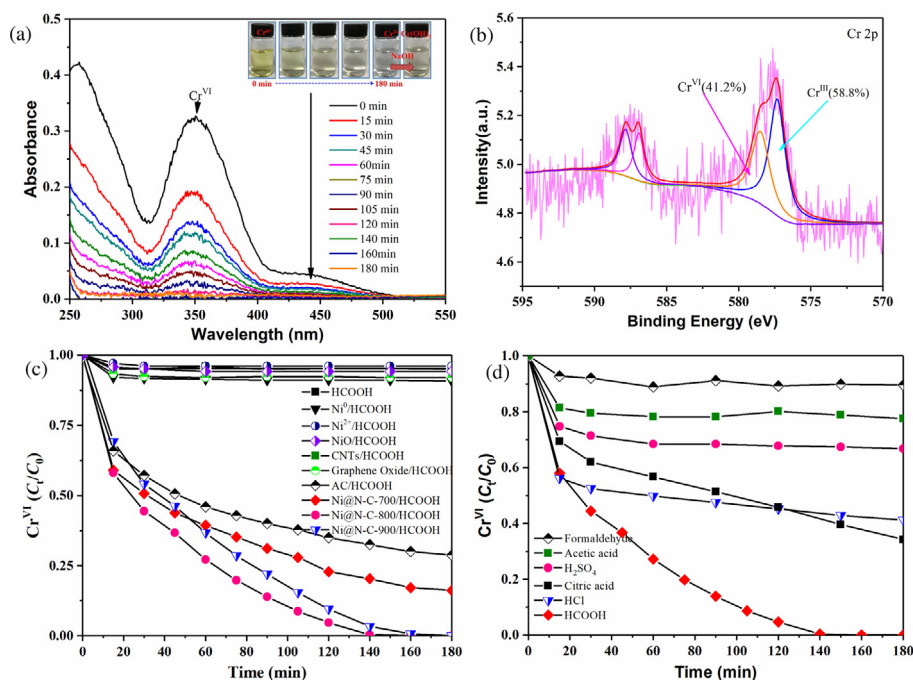


Fig. 7. (a) Typical time-dependent UV–vis absorption spectra of Cr^{VI} solution in Ni@N-C-800/HCOOH system. (b) Cr 2p XPS spectra of spent Ni@N-C-800 with the adsorbed Cr^{VI} species. Comparison of the catalytic performance in the presence of (c) different catalysts or (d) different reducing agents. Reaction conditions: [Cr^{VI}] = 10 mg/L, [catalyst] = 50 mg/L, T = 25 °C, [HCOOH] = 0.117 M.

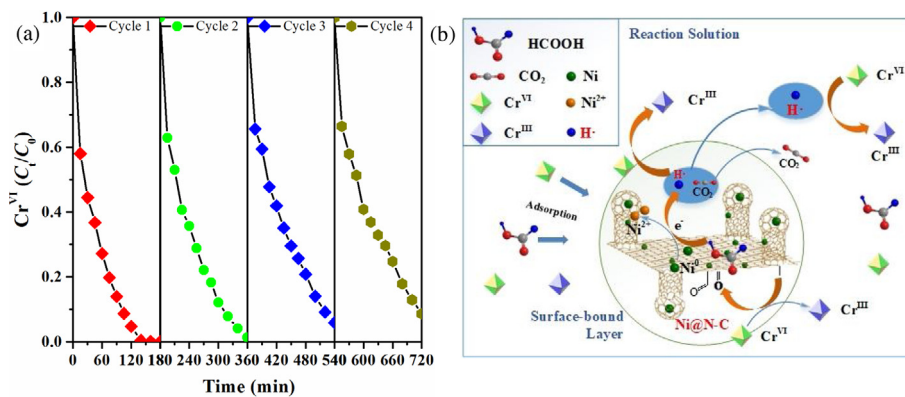


Fig. 8. (a) Repeated runs of Cr^{VI} reduction in Ni@N-C-800/HCOOH system. (b) Cr^{VI} reduction mechanism by Ni@N-C/HCOOH system. Reaction conditions: [Cr^{VI}] = 10 mg/L, [catalyst] = 50 mg/L, T = 25 °C, [HCOOH] = 0.117 M.

fact demonstrates hydrogen radical or atomic hydrogen is involved in Cr^{VI} reduction.

Based on the above analyses and discussion, a plausible mechanism for this redox reaction was proposed (Fig. 8b). In the solution, potassium dichromate exists mostly in the anionic form as HCrO_4^- , $\text{Cr}_2\text{O}_7^{2-}$, and CrO_4^{2-} ions. Initially, both formic acid and Cr^{VI} ions were firstly enriched on the surface of Ni@N-C by simple electrostatic attraction, where formic acid underwent a dehydrogenation decomposition pathway to produce CO₂ and hydrogen (H[•]) [49,50]. Ni⁰ has a strong enrichment capacity for hydrogen molecules, which could enhance the formation of atomic hydrogen [51]. In the presence of electron donating acids, the transformation of Cr^{VI} to less toxic Cr^{III} by the free hydrogen atom occurred [52]. It is noteworthy that Ni@N-C with an excellent electron transfer property could rapidly transfer the electron to reduce Cr^{VI}, which may be responsible for an improved catalytic activity. For Ni⁰ NPs, there was no electron-transfer mediator to promote the electron transfer. It might explain pure Ni⁰ has a lower reduction level compared to that of Ni@N-C. Hence, Ni@N-C exhibits superior electrochemi-

cal activities toward Cr^{VI} reduction due to the abundant active sites and effective electron transfer.

4. Conclusion

In this study, we demonstrated a facile, economic, and environmentally friendly method to fabricate novel “sea urchin”-like Ni@N-C 3D composites via an efficient thermal condensation of low-cost biomass, dicyandiamide and $\text{NiCl}_2 \cdot 6\text{H}_2\text{O}$. The physico-chemical characterizations including SEM, XRD, and TEM verified that large amounts of CNTs encapsulating Ni NPs had grown on AC sheets, revealing the effectiveness of the synthesis method. Additionally, the as-grown Ni@N-C exhibited excellent catalytic activity and stability for the degradation of organic dyes, and the reduction of aqueous toxic Cr^{VI} to nontoxic Cr^{III}, owing to the rationally designed microporous structure and more active catalytic sites. Detailed results indicated that the pyrolysis temperatures affected the compositions, morphologies, and catalytic properties of Ni@N-C composites. Furthermore, benefiting from the 3D porous structure,

the low cost of the precursors, and green methodology, the obtained highly active Ni@N-C catalysts offered very attractive prospects and could be extended toward practical applications.

ACKNOWLEDGEMENTS

The financial supports by National Natural Science Foundation of China (Grant 51372062), the Anhui Provincial Natural Science Foundation (NO. 1708085MB41) and the China Postdoctoral Science Foundation (NO. 2015M570547, 2016T90585) are acknowledged. A partial support from the Australian Research Council for DP150103026 is also acknowledged.

The authors declare no competing financial interest.

Appendix A. Supplementary data

Supplementary data associated with this article can be found, in the online version, at <http://dx.doi.org/10.1016/j.apcatb.2017.07.064>.

References

- [1] J. Su, Y. Zhang, S. Xu, S. Wang, H. Ding, S. Pan, G. Wang, G. Li, H. Zhao, *Nanoscale* 6 (2014) 5181–5192.
- [2] Y. Choi, M.S. Koo, A.D. Bokare, D.-h. Kim, D.W. Bahnemann, W. Choi, *Environ. Sci. Technol.* 51 (2017) 3973–3981.
- [3] F. Jing, R. Liang, J. Xiong, R. Chen, S. Zhang, Y. Li, L. Wu, *Appl. Catal. B: Environ.* 206 (2017) 9–15.
- [4] F.-Q. Shao, J.-J. Feng, X.-X. Lin, L.-Y. Jiang, A.-J. Wang, *Appl. Catal. B: Environ.* 208 (2017) 128–134.
- [5] F. Xu, R.D. Webster, J. Chen, T.T.Y. Tan, P.H.L. Sit, W.Y. Teoh, *Appl. Catal. B: Environ.* 210 (2017) 444–453.
- [6] D. Xia, Y. Li, G. Huang, R. Yin, T. An, G. Li, H. Zhao, A. Lu, P.K. Wong, *Water Res.* 112 (2017) 236–247.
- [7] A.V. Desai, B. Manna, A. Karmakar, A. Sahu, S.K. Ghosh, *Angew. Chem. Int. Ed.* 55 (2016) 7811–7815.
- [8] L. Luo, D. Wu, D. Dai, Z. Yang, L. Chen, Q. Liu, J. He, Y. Yao, *Appl. Catal. B: Environ.* 205 (2017) 404–411.
- [9] W.-D. Oh, Z. Dong, T.-T. Lim, *Appl. Catal. B: Environ.* 194 (2016) 169–201.
- [10] Y. Wang, Z. Ao, H. Sun, X. Duan, S. Wang, *Appl. Catal. B: Environ.* 198 (2016) 295–302.
- [11] J. Wang, Z. Wei, Y. Gong, S. Wang, D. Su, C. Han, H. Li, Y. Wang, *Chem. Commun.* 51 (2015) 12859–12862.
- [12] N. Karousis, I. Suarez-Martinez, C.P. Ewels, N. Tagmatarchis, *Chem. Rev.* 116 (2016) 4850–4883.
- [13] Z. Wei, J. Wang, S. Mao, D. Su, H. Jin, Y. Wang, F. Xu, H. Li, Y. Wang, *ACS Catal.* 5 (2015) 4783–4789.
- [14] Y. Yao, H. Chen, J. Qin, G. Wu, C. Lian, J. Zhang, S. Wang, *Water Res.* 101 (2016) 281–291.
- [15] Y. Yao, H. Chen, C. Lian, F. Wei, D. Zhang, G. Wu, B. Chen, S. Wang, *J. Hazard. Mater.* 314 (2016) 129–139.
- [16] K. Bhowmik, A. Mukherjee, M.K. Mishra, G. De, *Langmuir* 30 (2014) 3209–3216.
- [17] M. Li, Y. Xiong, X. Liu, C. Han, Y. Zhang, X. Bo, L. Guo, *J. Mater. Chem. A* 3 (2015) 9658–9667.
- [18] X.-L. Wu, T. Wen, H.-L. Guo, S. Yang, X. Wang, A.-W. Xu, *ACS Nano* 7 (2013) 3589–3597.
- [19] Z.-Y. Wu, C. Li, H.-W. Liang, J.-F. Chen, S.-H. Yu, *Angew. Chem. Int. Ed.* 52 (2013) 2925–2929.
- [20] H.U. Lee, S.C. Lee, Y.-C. Lee, S. Vrtnik, C. Kim, S. Lee, Y.B. Lee, B. Nam, J.W. Lee, S.Y. Park, S.M. Lee, J. Lee, *J. Hazard. Mater.* 262 (2013) 130–136.
- [21] M.A. Khalily, H. Eren, S. Akbayrak, H.H. Susapto, N. Biyikli, S. Özkar, M.O. Güler, *Angew. Chem. Int. Ed.* 55 (2016) 12257–12261.
- [22] C. Wan, J. Li, *ACS Sustainable Chem. Eng.* 3 (2015) 2142–2152.
- [23] J. Shi, Y. Wang, W. Du, Z. Hou, *Carbon* 99 (2016) 330–337.
- [24] Y. Yao, J. Zhang, G. Wu, S. Wang, Y. Hu, C. Su, T. Xu, *Environ. Sci. Pollut. Res.* 24 (2017) 7679–7692.
- [25] Y. Zhao, J. Zhang, K. Li, Z. Ao, C. Wang, H. Liu, K. Sun, G. Wang, *J. Mater. Chem. A* 4 (2016) 12818–12824.
- [26] H. Song, H. Cui, C. Wang, *ACS Appl. Mater. Interfaces* 6 (2014) 13765–13769.
- [27] M. Ma, S. You, W. Wang, G. Liu, D. Qi, X. Chen, J. Qu, N. Ren, *ACS Appl. Mater. Interfaces* 8 (2016) 32307–32316.
- [28] F. Luo, Z. Chen, M. Megharaj, R. Naidu, *Chem. Eng. J.* 294 (2016) 290–297.
- [29] C. Wang, G. Shao, Z. Ma, S. Liu, W. Song, J. Song, *Electrochim. Acta* 130 (2014) 679–688.
- [30] S. Li, L. Tang, G. Zeng, J. Wang, Y. Deng, J. Wang, Z. Xie, Y. Zhou, *Environ. Sci. Pollut. Res.* 23 (2016) 22027–22036.
- [31] Y. Huang, Y. Liang, Y. Rao, D. Zhu, J.-j. Cao, Z. Shen, W. Ho, S.C. Lee, *Environ. Sci. Technol.* 51 (2017) 2924–2933.
- [32] F. Lai, Y.-E. Miao, Y. Huang, Y. Zhang, T. Liu, *ACS Appl. Mater. Interfaces* 8 (2016) 3558–3566.
- [33] W. Tian, H. Zhang, X. Duan, H. Sun, M.O. Tade, H.M. Ang, S. Wang, *ACS Appl. Mater. Interfaces* 8 (2016) 7184–7193.
- [34] J. Yin, Q. Fan, Y. Li, F. Cheng, P. Zhou, P. Xi, S. Sun, *J. Am. Chem. Soc.* 138 (2016) 14546–14549.
- [35] J.S. Cho, S.Y. Lee, H.S. Ju, Y.C. Kang, *ACS Appl. Mater. Interfaces* 7 (2015) 25641–25647.
- [36] C. Zhou, J.A. Szpunar, X. Cui, *ACS Appl. Mater. Interfaces* 8 (2016) 15232–15241.
- [37] P.K. Boruah, P. Borthakur, G. Darabdhara, C.K. Kamaja, I. Karbhal, M.V. Shelke, P. Phukan, D. Saikia, M.R. Das, *RSC Adv.* 6 (2016) 11049–11063.
- [38] T. Chen, B. Cheng, G. Zhu, R. Chen, Y. Hu, L. Ma, H. Lv, Y. Wang, J. Liang, Z. Tie, Z. Jin, J. Liu, *Nano Lett.* 17 (2017) 437–444.
- [39] X. Li, Z. Ao, J. Liu, H. Sun, A.I. Rykov, J. Wang, *ACS Nano* 10 (2016) 11532–11540.
- [40] H. Lee, H.-i. Kim, S. Weon, W. Choi, Y.S. Hwang, J. Seo, C. Lee, J.-H. Kim, *Environ. Sci. Technol.* 50 (2016) 10134–10142.
- [41] J. Chen, L. Zhang, T. Huang, W. Li, Y. Wang, Z. Wang, *J. Hazard. Mater.* 320 (2016) 571–580.
- [42] J. Zhang, X. Shao, C. Shi, S. Yang, *Chem. Eng. J.* 232 (2013) 259–265.
- [43] G. Liu, S. You, Y. Tan, N. Ren, *Environ. Sci. Technol.* 51 (2017) 2339–2346.
- [44] X. Cheng, H. Guo, Y. Zhang, X. Wu, Y. Liu, *Water Res.* 113 (2017) 80–88.
- [45] C. Wang, J. Kang, P. Liang, H. Zhang, H. Sun, M.O. Tade, S. Wang, *Environ. Sci.: Nano* 4 (2017) 170–179.
- [46] H. Lee, H.-J. Lee, J. Jeong, J. Lee, N.-B. Park, C. Lee, *Chem. Eng. J.* 266 (2015) 28–33.
- [47] B. Jiang, X. Wang, P. Hu, M. Wu, J. Zheng, W. Wu, *Chemosphere* 144 (2016) 1611–1617.
- [48] F. Gong, L. Luo, Y. Yao, D. Dai, W. Lu, W. Chen, *Chem. Eng. J.* 304 (2016) 440–447.
- [49] M. Liang, R. Su, W. Qi, Y. Zhang, R. Huang, Y. Yu, L. Wang, Z. He, *Ind. Eng. Chem. Res.* 53 (2014) 13635–13643.
- [50] Y. Guo, D. Wang, X. Liu, X. Wang, W. Liu, W. Qin, *New J. Chem.* 38 (2014) 5861–5867.
- [51] X. Zhou, G. Jing, B. Lv, Z. Zhou, R. Zhu, *Chemosphere* 160 (2016) 332–341.
- [52] A.K. Mishra, D. Pradhan, *Cryst. Growth Des.* 16 (2016) 3688–3698.